# Microfiber analysis via femtosecond stimulated Raman microscopy (FSRM)

Carolin Borbeck, Francisco van Riel Neto, Roman Bernst & Peter Gilch



Suggested Citation:
Borbeck, C., van Riel Neto, F., Bernst, R., & Gilch, P. (2025). Microfiber analysis via femtosecond stimulated Raman microscopy (FSRM). Microplastics and Nanoplastics, 5, Article 14. https://doi.org/10.1186/s43591-025-00113-0

Microplastics and Nanoplastics

RESEARCH Open Access

# Microfiber analysis *via* femtosecond stimulated Raman microscopy (FSRM)

Carolin Borbeck[1], Francisco van Riel Neto[1], Roman Bernst[1] and Peter Gilch[1*]

**Abstract**
Small polymeric particles termed microplastics have become ubiquitous in the environment. They are found in various shapes, among which microfibers are emerging as the most abundant type. Assessing the contamination of aqueous ecosystems with synthetic microfibers requires a clear distinction from natural ones. Here, we introduce femtosecond stimulated Raman microscopy (FSRM) for fast analysis of microplastics in water, particularly microfibers. Utilizing FSRM, fabric samples of both synthetic and natural origin were analyzed. Spatial and nearly complete (1000–3500 $cm^{-1}$) spectral information on the particles is obtained. Raman images consisting of 40,000 spatial pixels and covering an area of $200 \times 200$ $\mu m^2$ are obtained within seven minutes.

**Keywords** Microfibers, Microplastics monitoring, Non-linear Raman microscopy

## Introduction

Plastics have been part of our daily lives for many decades and their usage keeps increasing [1]. A recent OECD report estimates its use to triple until 2060 compared to 2019 if no policy changes are implemented [2]. Among other characteristics, plastics are cheap to produce, durable, and lightweight, making them accessible for different usages in various industries, e.g., reducing energy consumption in transport by replacing materials with higher density [3]. However, plastics are currently being criticized due to harmful impacts both on the environment and human well-being. Special emphasis has been laid on the issue of microplastics (MP), which are small pieces of synthetic polymers with a suggested upper size limit of 5 mm [4]. They were first explicitly mentioned and termed in 2004 [5], although earlier reports of such small particles exist [6]. Microplastics have become ubiquitous and have been documented across various environmental settings [5, 7–10].

In a 2014 study, it was modeled that more than 250,000 tons of plastic float in the oceans of the world, among which approximately 35,500 tons are due to particles below 5 mm [11]. There is evidence for an upward transfer along the food chain, with documented instances of microplastics in aliments such as beer [12] and drinking water [13] as well as condiments, honey, vegetables, meat, and seafood [14]. By ingestion they can be admitted into the body and were detected in various human specimen, including human blood [15], placenta [16, 17], breast milk [18], meconium [17], and lung tissue [19, 20]. The implications of microplastic exposure on health are only partially known, however a recent study suggests a change in the behavior of mice upon exposure to microplastics [21].

Fibers are the most abundant shape of MP particles found in the environment, followed by fragments and others, for example beads or foams [22]. A major source for these particles in the environment is laundry of synthetic textiles [23]. In 2022, synthetic fibers made up 65% of the global fiber production [24]. Polyester is the most

*Correspondence:
Peter Gilch
gilch@hhu.de
[1]Institut für Physikalische Chemie, Heinrich-Heine-Universität Düsseldorf, Universitätsstr. 1, 40225 Düsseldorf, Germany

common material used in the production of fibers worldwide, followed by cotton, polyamide, and viscose, a man-made cellulosic fiber [24]. Chemical and physical stress on the fabric during the washing cycle results in the release of microfibers which often cannot be extracted during the treatment of wastewater. They are therefore released into the environment. During the washing cycle, more than 100 fibers are released per liter of effluent water [9].

However, recent reports suggest that the number of MP fibers reported in environmental samples is overestimated and that only 22% of fibers found are actually of synthetic origin [25], pointing out the importance of both quantitative and qualitative analytics. Further overestimates were reported in the case of beverages: As mentioned above, synthetic particles were found in beer [12] and drinking water [13], but when specifically investigating fibers in beverages, no synthetic particles were detected [26]. Here, mostly cellulose fibers were found. Furthermore, blank samples displayed a comparable number of particles present as in samples. This emphasized not only the omnipresence of microfibers but also the need for sample preparation protocols and adequate qualitative analysis of samples.

Visual identification is often applied as a means of quantitative MP identification or pre-selection for further analytics but can only be applied sufficiently accurate for particles larger than ~ 1 mm [27]. One important tool for qualitative evaluation of particles often applied in microplastics analysis is vibrational spectroscopy (Raman or IR). It delivers information on the chemical composition of a sample and the methods are often combined with microscopy to acquire qualitative and quantitative information simultaneously. Spectra for several positions in a sample region are recorded. The position dependent spectra can be transformed into "chemical maps" using various algorithms to describe shape and composition of microparticles. From here on, only chemical maps resulting from Raman spectral information will be discussed and therefore termed Raman maps for the sake of clarity.

Both Raman- and IR-micro-spectroscopy have been applied in the analysis of MP particles and both show relevant advantages and disadvantages depending on the application [28]. For linear techniques of vibrational spectroscopy, IR spectroscopy is generally faster than Raman spectroscopy due to higher cross sections [29]. Furthermore, the (laser) light employed to induce Raman scattering may also trigger fluorescence emission which can surmount the Raman signals [28]. As mostly aqueous samples are investigated for MP contamination, strong IR cross sections of water may be a challenge [30]. In contrast, water is a weak Raman scatterer [31]. Furthermore, due to the higher lateral resolution of Raman spectroscopy of ~ 1 µm compared to that of IR spectroscopy of ~ 10 µm [32], smaller particles can be identified. These values are based on the Abbe diffraction limit [33] assuming large aperture objectives ($A_{num} \approx 1$) and typical wavelengths for the two techniques. The higher resolution of Raman spectroscopy proves especially helpful in micro-spectroscopy. Unfortunately, the aforementioned low scattering cross sections of Raman scattering lead to long measurement times for the generation of Raman maps of samples at hand.

Non-linear approaches like stimulated Raman scattering (SRS) aim to increase the speed of vibrational Raman (micro-)spectroscopy. As shown schematically in Fig. 1, in the most common implementation of SRS [34–36], a Raman vibration is stimulated by two narrowband pulses of different wavenumbers [35, 37]. Traditionally, in SRS, these beams are referred to as Stokes and pump, corresponding to the laser light with lower and higher energies, respectively. In the context of this study the standard notation for femtosecond stimulated Raman scattering (FSRS) will be employed [38]. In FSRS, one utilizes a weak broadband pulse termed Raman probe and an intense narrow bandwidth one termed Raman pump. In our implementation, the probe pulse is on the high frequency side with respect to the pump. When in SRS the Raman condition is met, i.e. the wavenumber difference between the pump and probe beams matches the wavenumber of a Raman transition, photons of the higher energy beam are annihilated (stimulated Raman loss, SRL), while photons of the lower energy beam are generated (stimulated Raman gain, SRG) [35]. These changes in power can subsequently be detected. In "traditional" SRS, for each Raman active mode to be addressed, the wavenumber difference between the two lasers needs to be adjusted. Acquisition of a complete Raman spectrum, thus, requires tuning the wavenumbers of Raman pump or probe. The stimulated Raman effect has a much larger effective cross section than the spontaneous one [29], thus decreasing the acquisition time necessary for a sufficiently high signal-to-noise ratio. In addition to the reduction in acquisition time, the issue of disturbing fluorescence background is mitigated [39]. Fluorescence occurs at lower energies than used for the excitation. If Raman loss of the higher energy laser is recorded for generation of the SRS spectra, fluorescence effects are thus rendered irrelevant.

SRS microscopy was already successfully applied to MP characterization [40, 41]. At pre-selected Raman shifts, signals at several positions of a sample were recorded, yielding a Raman map of the MP distribution. For a given sample size, a full spatial map can be recorded. If full spectral information is to be obtained as well, several successive measurements need to be performed, always probing different wavenumbers of the Raman spectrum. Only few characteristic Raman bands were probed in the

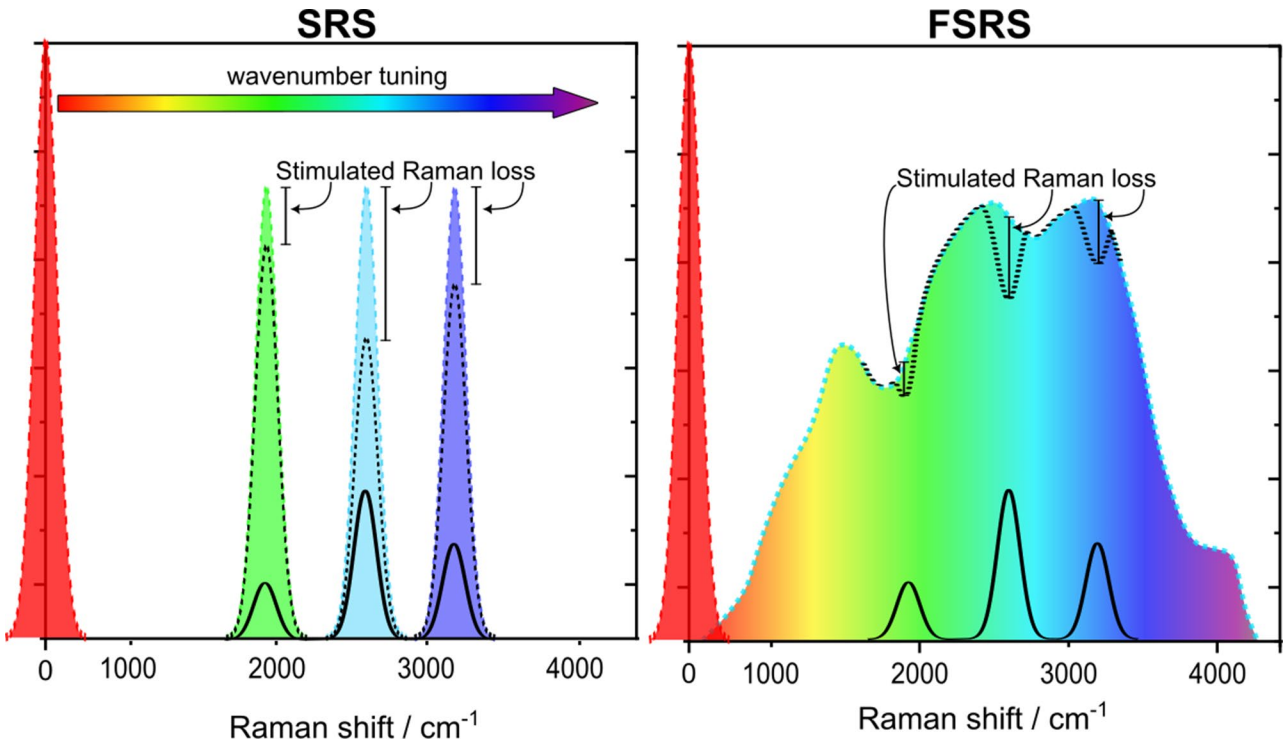


**Fig. 1** Two modalities of SRS. In the most common implementation of SRS (left) two narrow bandwidth laser pulses are employed. Their wavenumber difference (Raman shift) is tuned to meet the Raman conditions (schematic Raman spectrum in black). The high frequency pulse (green to blue colors) will decrease in intensity due to the SRS process. From this decrease the Raman signal can be evaluated. Addressing different Raman bands requires tuning of the wavenumber difference. In FSRS (right) a narrow bandwidth Raman pump pulse (red) and broadband probe (rainbow color gradient) are employed. Raman resonances show up as small dips in the probe spectrum. From these dips the Raman spectrum is obtained. The depicted shape and Raman shifts of the probe pulse represent the properties of the pulse in the present experiments

study. SRS was also applied specifically for microfibers [25, 42]. In that example, microscopical images of fibers were recorded and a full SRS spectrum within a spectral range of 800–3200 $cm^{-1}$ was obtained for one selected point of interest by scanning the wavenumber difference. Thus, when employing SRS microscopy, one commonly compromises concerning spatial and/or spectral coverage. FSRS [37, 43] is based on the same non-linear process. However, a broadband Raman probe pulse is employed (Fig. 1). Its spectral width equals approximately the largest Raman shift of common molecules [44]. This enables the simultaneous detection of all Raman signals by recording the changes in the probe spectrum induced by SRS.

We here introduce femtosecond stimulated Raman microscopy (FSRM) as a fast, broadband tool for simultaneously acquiring quantitative and qualitative information about samples containing microfibers. FSRM was invented by our group in 2007 [36]. In its present implementation, acquisition times per spectrum as short as 0.1 ms are possible [45, 46]. The technique is based on FSRS [37, 43]. In our setup, the Raman probe has a higher wavenumber than the narrow-band Raman pump and will therefore experience stimulated Raman loss for all wavenumbers where the difference in wavenumber between pump and probe matches that of a Raman active mode (see Fig. 1). The setup provides complete Raman spectra. Thus, prior knowledge of the sample and its expected Raman active modes is not necessary. Notably, the technique does not require high laser powers, ensuring a destruction-free and fast acquisition of Raman maps even for sensitive samples [45]. In addition to Raman signatures, also transmission information without the need for additional scanning is obtained.

To demonstrate the capabilities of FSRM with respect to microfiber analytics, we selected samples for prevalent types of fabrics produced worldwide [47] of both synthetic and natural origin. We will prove that a direct determination of the type of fiber found in a sample is possible without any necessary pre-selection or pre-evaluation. Polyester, commonly found in the form of polyethylene terephthalate (PET), is the fabric with the highest production volume in 2022 [24]. Nylon was included as an additional example of a synthetic fiber. Linen was chosen to represent common cellulosic fibers. Finally, despite its relatively low global production percentage, wool serves as an example of a fabric of animal origin. For all samples, a preparation protocol was

developed to mimic handling samples from aqueous environments. FSRM enables an immediate distinction between the fabric types. The method chosen for data evaluation here was a fuzzy c-means clustering algorithm (FCM). As full spectral coverage is achieved, other methods like k-means clustering, hierarchical clustering, or principal component analysis (PCA) [48] could be applied as well but lie outside of the scope of this report. To conclude our analysis, a denim fabric primarily composed of cotton and polyester underwent examination with FSRM. In this case, a bleaching step was introduced to enable adequate transmission and mitigate non-linear effects other than SRS, for example transient absorption, arising from the blue dye.

## Materials and methods

### FSRM microscope

The most important current features of the FSRM setup will be given here. More detailed information can be found in the references [45, 49]. A Ti:Sa laser (Femtolasers, Fusion BB 400) is used for the generation of both Raman pump and Raman probe pulses. Its output is centered around 810 nm with a spectral width of approximately 120 nm (FWHM), an average light power of approximately 440 mW, and a repetition rate of 75 MHz. The laser light can be directly used as the Raman probe pulse, it will only pass two sets of chirped mirrors to pre-compensate the temporal chirp which will be added by the microscope objectives. Due to the broad spectra of the fs-laser, Raman signals in the range 850 to 4000 $cm^{-1}$ can be recorded. This is possible because its spectrum deviates from a Gaussian profile, maintaining sufficient spectral intensity not only within the FWHM range (~ 1260 $cm^{-1}$ to 3100 $cm^{-1}$) but also beyond it [49]. Fig. 1 provides a schematic representation of the probe spectrum. Before focusing on the sample, the power is reduced to around 2 mW, mostly to avoid saturation of the detector.

The Raman pump pulse is generated by coupling a portion of the laser light (wavelengths > 950 nm) into a customized fiber amplifier. Even around 950 nm, the laser light has sufficient spectral power to seed the fiber amplifier (200 µW). The amplifier is based on $Yb^{3+}$ doped fibers and leads to an amplification of the pulsed seed light at 977 nm. The amplified light exhibits an average power of 32 mW with a FWHM of ~ 30 $cm^{-1}$, which determines the spectral resolution. An accousto-optic modulator integrated in the amplifier switches the train of pump pulses on and off at a frequency half the readout rate of the detector. A modulation of the pump power is included preventing damage to samples [45]. Raman pump and probe are recombined and guided into a microscope objective (Zeiss, Fluar, 20x NA 0.75) to be focused onto the sample which is placed on a movable xy-stage for scanning. The transmitted light is collected by a second objective (Zeiss, Achroplan, 100x NA 1.25), and the pump light is filtered out using a shortpass-filter. The probe light is guided into a polychromator where it is spectrally dispersed and detected by a multi-channel detector with 512 pixels and a readout rate of 20 kHz (Quantum Detectors, ULTRA).

The detector provides signals as a function of probe wavelength $\lambda_{Pr}$ alternately in presence $S_{\mathrm{Probe+Pump}}$ and absence $S_{\mathrm{Probe}}$ of the Raman pump light. The probe wavelength is converted into Raman shift $\tilde{\nu}$ via Eq. (1),

$$\tilde{\nu} = \frac{1}{\lambda_{Probe}} - \frac{1}{\lambda_{Pump}}. \tag{1}$$

Here, $\lambda_{\mathrm{Pump}} = 977$ nm is the central wavelength of the pump light. The Raman spectra $R\left(\tilde{\nu}\right)$ are computed from the detector signals by referencing the signals via Eq. (2),

$$R\left(\tilde{\nu}\right) = 1 - \frac{S_{Probe+Pump}\left(\tilde{\nu}\right)}{S_{Probe}\left(\tilde{\nu}\right)}. \tag{2}$$

For the generation of the spatial map, the xy-stage on which the sample is mounted is moved in a zigzag pattern with steps of a given length. The movement of the stage is continuous and its speed is adjusted according to the number of total spectra which are to be averaged for the measurement. Finally, separate Raman spectra are computed for each sample position, with each spectrum representing one "step" of the microscope stage. For the measurements shown here, 100 Raman spectra (equal to 200 probe spectra) were averaged for each pixel position with each step being 1 µm. A total range of 200 µm was covered in both directions.

The probe spectra recorded for the generation of the Raman spectral map can also be used for the calculation of a transmission map. The probe spectra recorded at each position $S_{\mathrm{probe,\,sample}}$ were averaged and the transmission for each position is calculated based on an initial spectrum of water $S_{\mathrm{probe,\,water}}$ recorded before starting a scan. In the respective transmission maps, the averaged transmission for the whole spectrum (512 pixels) was plotted (Eq. (3)),

$$T = \frac{1}{512}\sum_{i=1}^{512}\frac{S_{\mathrm{Probe,\,sample}}\left(\tilde{\nu}_i\right)}{S_{\mathrm{Probe,\,water}}\left(\tilde{\nu}_i\right)}. \tag{3}$$

Here, $\tilde{\nu}_i$ are wavenumbers assigned to the 512 elements of the array detector.

## Sample preparation

Undyed fabric samples were chosen for this study as measurements with FSRM are conducted in transmission and absorption of light by dyes or pigments should be avoided. The chosen samples were nylon, polyester, and linen acquired from *Stoffe Wolle Kurzwaren Weinreich, Düsseldorf, Germany*. A sample of wool fabric was acquired from *Axel Suijker Textil, Quakenbrück, Germany*. A sample of denim fabric was acquired from a used pair of jeans consisting of 69% cotton, 26% polyester, 4% viscose, and 1% elastane.

Approximately 0.6 mg of the respective fabric was cut into pieces as small as possible using scissors. The pieces were further dissected into smaller particles by placing them in distilled water and tearing them apart using two spatulas. The liquid including the particles was transferred to a volumetric flask and shaken for 3 min. Then, it was filtrated over an aluminum oxide filter (0.2 µm, Whatman®, Anodisc®, 25 mm Ø). This filter was chosen for being transmissive when wet and it does not feature disturbing Raman signals in the relevant wavenumber regions [50]. The wet filter was then placed on an object slide (40 × 60 mm, #1 thickness) and covered with a round cover slip (25 mm Ø). As the filter needs to be thoroughly wet for the measurement, some water was added between the cover slips with an Eppendorf® pipette. Afterwards, the sides of the top cover slip were sealed using clear nail polish to prevent evaporation of water.

For the measurements of the bleached denim fabric, sodium hypochlorite was chosen as a bleaching agent. This is a possible step in a procedure to extract microplastic from soil organic matter without substantial damage to the plastic [51]. The fabric was soaked in distilled water for 30 min and then transferred to a 6.5% NaOCl solution based on the sample preparation described in ref. [52]. The fabric was found to be visibly discolored after 2 h of bleaching. The fabric was then washed with distilled water over a filter and finally a sample was prepared as described above.

### Data analysis

Visualizations of different aspects of the spectral data were performed using the commercially available software *ImageLab*®. In this study, spectral descriptors were defined. To this end, the Raman spectrum was inspected and baseline corrected integrals covering representative Raman bands computed. These integrals serve as descriptors. The following evaluations by means of clustering algorithms were based on these manually defined descriptors. For a list of the descriptors used and their assigned Raman vibrational modes, see Supporting Information (Table S1). Employing the complete Raman spectral information proved problematic. For the samples investigated, Raman bands are sparsely distributed over the relevant spectral range. Thus, the spectral data is dominated by baseline contributions and their fluctuations. Such an analysis mostly recovers these fluctuations and was therefore not performed here.

The approach used for clustering of the spectra within a map shown here was the fuzzy c-means clustering algorithm. This algorithm assigns each sample point a similarity with a cluster. This similarity is expressed as a function with a value between 0 and 1 [53]. An averaged spectrum for all points assigned to one cluster was calculated.

The number of clusters was pre-selected before the analysis. In this case, it was known prior to evaluations how many different types of fibers were seen in a map. The number of clusters chosen must be at least the number of types of fibers present plus one cluster for water. Selecting an additional cluster to identify regions with low transmission leading to high noise increased the quality of the acquired image as well as the averaged spectra within the clusters. This "distortion" cluster describes regions of the fiber that lie outside of the focal plane (cf. Fig. 3).

## Results

### FSRM Raman spectra of selected white fabrics

First, reference Raman spectra of the selected fabrics were recorded. In these measurements no scanning was performed so that the size of these specific fibers was not quantified. The two laser beams were focused on a single position in a fiber and the focusing conditions were optimized for maximum Raman signal at this position. The probe light was maximized until almost saturation of the detector to decrease noise levels. At the maximum of the probe spectrum (~ 810 nm, Raman shift of 2140 $cm^{-1}$), this leads to a detected number of ~ $6.2 \times 10^7$ photons per readout (acquisition time 50 µs) [49]. Reference spectra averaging a total of 10,000 spectra were recorded within 1 s for the synthetic and natural fibers (Fig. 2), considering that the acquisition of one Raman spectrum requires two readouts. The spectra $S_{probe+pump}$ and $S_{probe}$ are averaged separately. Therefore, the shot noise SN can be calculated based on a total of $N \approx 6.2 \times 10^{11}$ photons (Eq. 4),

$$SN = \frac{1}{\sqrt{N}} = 1.3\text{x}10^{-6}. \quad (4)$$

In a spectral region free of Raman bands (1790–2558 $cm^{-1}$), on average, a relative standard deviation of $7.4 \times 10^{-6}$ is computed for the four spectra shown. The ~ 5-fold increase compared to the shot noise limit is presumably due to optical distortions by the fiber.

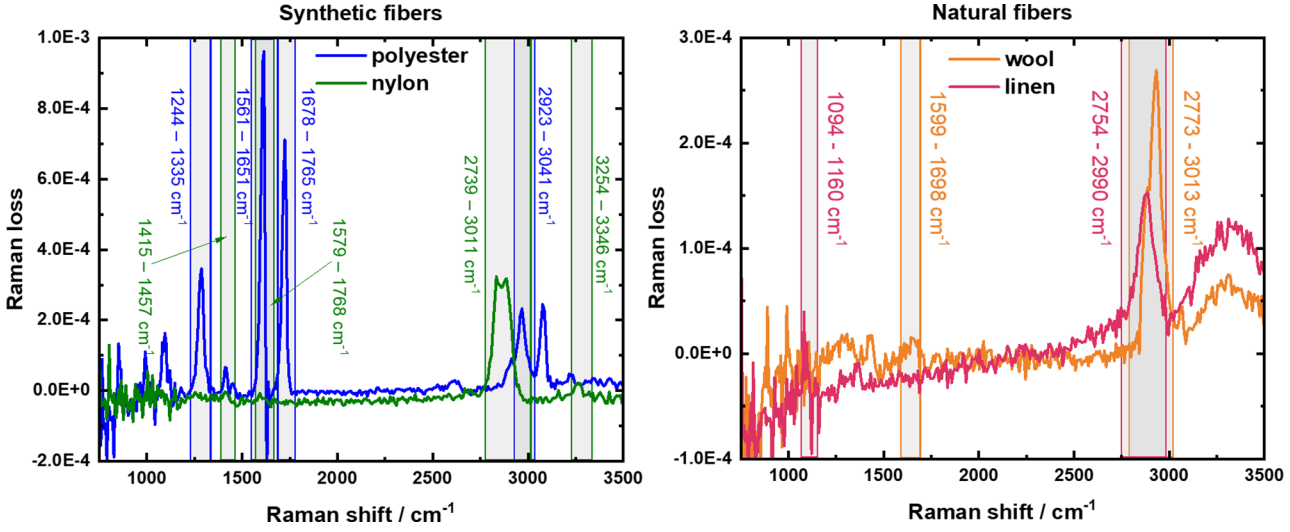


**Fig. 2** FSRM Raman spectra of synthetic (left) and natural origin (right) fibers recorded with an acquisition time of 1 s/spectrum, corresponding to 10,000 averaged spectra. The descriptors used for the FCM clustering analysis of the maps are marked in the respective colors of the spectra

The averaging time was chosen to acquire spectra with low noise. The signal to noise ratio of the most prominent Raman bands allows for shorter acquisition times, for example 10 ms. This is the chosen setting for each spectrum in the Raman maps recorded in this study. To illustrate the impact of acquisition times, reference spectra recorded for polyester averaging over 1 s and 10 ms are provided in the Supporting Information (Fig. S1).

The nylon and polyester fibers could be measured directly without addition of water as they are sufficiently transmissive for the probe light. However, linen and wool fibers were not transmissive without being soaked in water. The corresponding FSRM Raman spectra of the natural fibers therefore show the Raman signature of water in addition to those of the fibers, ranging from 3100 $cm^{-1}$ to 3600 $cm^{-1}$ [54].

The typical Raman bands of CH-stretching vibrations characteristic for many polymers are visible in all spectra around 3000 $cm^{-1}$ [55]. Matching observations from conventional Raman spectroscopy, these bands are the strongest in nylon, wool, and linen. The most prominent Raman bands used as descriptors for cluster analysis are marked in Fig. 2. These descriptors are summarized and assigned in Supporting Information Table S1 [55–58]. Additional Raman bands not used as descriptors are addressed here.

For polyester, a second Raman band attributable to aromatic CH bonds at 3077 $cm^{-1}$ is observed. The band centered at 2968 $cm^{-1}$ displays a shoulder, which is caused by CH stretching of the methylene sequences expected around 2895 $cm^{-1}$ [58]. Unlike the other specimen, the CH stretching vibrations are not the strongest Raman signals. Further vibrational signatures are found here at 1410 $cm^{-1}$ and 1451 $cm^{-1}$ (CH bending), 1179 $cm^{-1}$ (CC ring stretching), 1094 $cm^{-1}$ (CO and CC stretching), 990 $cm^{-1}$ (COC bending), and 851 $cm^{-1}$ (CC stretching) [56, 57]. For the aromatic CC ring stretching band centered at 1615 $cm^{-1}$, a negative wing can be observed on the higher-wavenumber side. This effect can occur in stimulated Raman if the pump-probe delay is slightly shifted from perfect temporal overlap [59], which seems to be the case here.

In the Raman spectrum of linen, which consists of cellulose, weak bands just above the noise level are detected in this study at 1465 $cm^{-1}$ ($CH_2$ bending scissors), 1382 $cm^{-1}$ ($CH_2$ and HCO bending), 1159 $cm^{-1}$ (CC and CO stretching of the glycosidic ring). Additional bands at 1341 $cm^{-1}$, 1334 $cm^{-1}$, and 1297 $cm^{-1}$ as reported in ref. [56, 57] are not observed here. Raman bands at lower wavenumbers cannot be observed due to increased noise levels.

Finally, for wool, which mainly consists of keratin, a peak expected around 3300 $cm^{-1}$ indicating NH stretching is likely masked by the broad band of OH vibrations of water [55, 57, 60]. Further Raman bands roughly at the noise level of the above measurement are found centered at 1515 $cm^{-1}$ (CH bending), 1437 $cm^{-1}$ ($COO^-$ bending), and 1307 $cm^{-1}$ ($CH_2$ bending) [57]. Raman bands at lower wavenumbers cannot be observed here. Note that a weak baseline shift observed here was not corrected for, as it does not substantially affect the spectrum.

### FSRM imaging of fibers

To obtain FSRM Raman maps, the sample was scanned while continuously recording Raman spectra. After focusing, the probe intensity was reduced by ~30% to avoid saturating the detector, especially while scanning the more transmissive water rich regions. This was

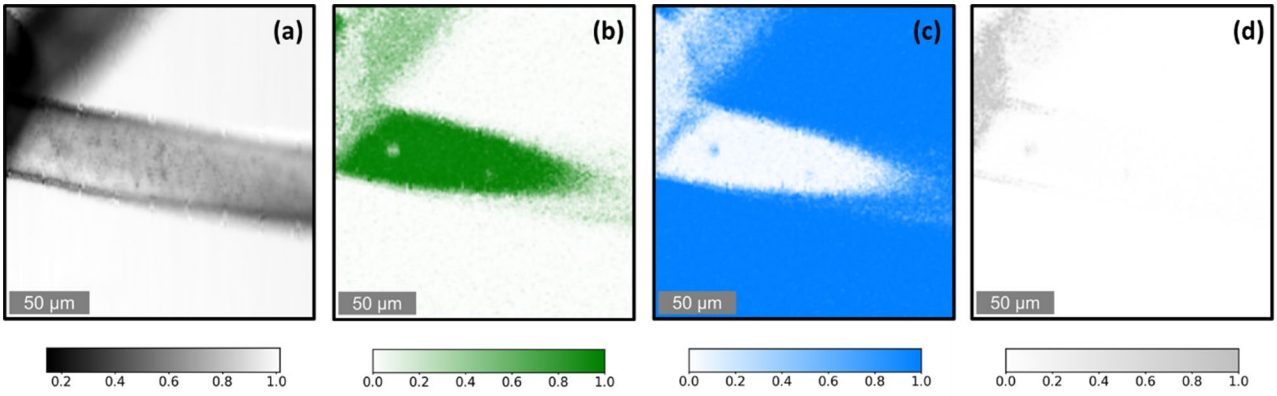


**Fig. 3** FSRM imaging of nylon fibers dispersed in water. The maps are recorded with an acquisition time of 10 ms per pixel (corresponding to 100 averaged spectra per pixel) with a spatial resolution of 1 µm. Acquisition of the 200 × 200 µm$^2$ map took ~ 7 min. The transmission map (**a**) was generated employing the FSRM data. The average transmission of the whole probe spectral range is shown in relation to a reference spectrum recorded in the water region of the sample. Darker shades indicate lower transmission. The assignments to the FCM clusters for nylon (**b**), water (**c**) and distortion (**d**) are color-coded for values between 0 (white) and 1 (full saturation). Regions with low transmission result in a higher distortion and the spectra in these regions are less likely to be assigned to a cluster of nylon or water

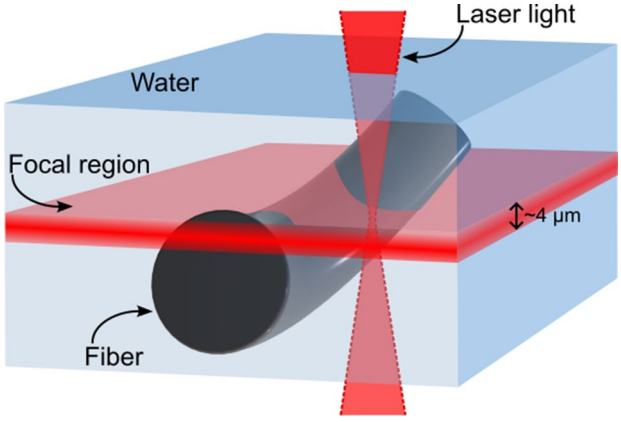


**Fig. 4** Sectioning capabilities of FSRM and its impact on fiber imaging. Due to its non-linear nature, SRS generates Raman signals mostly for objects in the focal plane or slightly above or below it. Fibers or parts of fibers outside this region will essentially not contribute to the Raman signal

necessary as usually more light is transmitted in the watery regions of the sample, resulting in more probe light arriving at the detector compared to focusing on the fiber. Unfortunately, this resulted in higher noise levels, especially in regions of lower transmission. An area of 200 × 200 µm$^2$ was scanned with steps of 1 µm. As scanning here involves the motion of the samples and not the laser spot, scanning speeds had to be limited to avoid displacements of the fibers in the sample. Pixel acquisition time was set to 10 ms/pixel, resulting in a total acquisition time per image of approximately 7 min.

A transmission map (Fig. 3(a)) computed from the FSRM data resembles a conventional micrograph. An approximately horizontally aligned fiber is clearly discernible. To visualize the fiber according to its Raman characteristics, the FCM clustering algorithm was used. The respective spectral descriptors can be found in the Supporting Information (Table S1). Based on the composition of the samples at least two clusters ought to be involved– one for nylon and one for water. For the description of the data, it proved beneficial to add another FCM cluster referred to as distortion cluster. This cluster accounts for regions with low transmission due to strong scattering, as described in the Materials and Methods section. (We note here that the number of clusters necessary could also be determined by principal component analysis.)

The region assigned to the FCM cluster for nylon (Fig. 3(b)) and thereby to the fiber is smaller than expected based on the transmission map (Fig. 3 (a)). This can be attributed to the sectioning capabilities of the SRS process [61]. SRS is mostly sensitive for material close to or within the focal plane of the microscope (Fig. 4). Assuming Gaussian optics [33], the depth of field is calculated to be approximately 4 µm. While this value was not experimentally verified, it aligns with the sectioning capabilities observed in this study. Thus, the part of the nylon fiber on the left is within the focal region, the right part not. The FCM cluster for water confirms this (Fig. 3 (c)). Trivially, water is mostly at positions where there are no fibers. Thus, the water map is the "negative" of the nylon map. On the right part of the nylon fiber (according to the transmission) water is observed, indicating that here the fiber is not in the focal region.

The diameter of the nylon fiber can be determined using the transmission map (Fig. 3(a)) or the Raman map (Fig. 3 (b)). As the transmission is lower on the edges of the fiber and, consequently, the Raman signal, the values slightly differ depending on which measurement is used. From the transmission map, a diameter of about 56 µm can be determined. For the Raman map, the diameter is slightly lower with 51 µm. These results were verified

by determining the diameter of a single nylon thread extracted from the fabric to be 50 µm using a sliding caliper. The results lie within the same range, which is to be expected as the nylon fibers did not disintegrate further during the sample preparation.

Raman spectra for positions assigned to each cluster were averaged and are shown in Fig. 5. They depict the same characteristics as the reference spectra recorded, however displaying a lower signal-to-noise ratio (SNR). Different scattering in different sample positions resulted in changing focusing conditions. As a result, the overlap of the pump and probe beams changed and, consequently, less stimulated Raman scattering occurred, ultimately decreasing the signal level of the averaged spectra.

Raman maps of all other reference fibers were recorded and evaluated in the same manner as for nylon (Fig. 6). The averaged cluster spectra show the same characteristic Raman bands as expected from the recorded reference spectra, enabling a distinction between different types of fibers. Water and "distortion" cluster images and spectra for these samples are not shown here (see Supporting Information Fig. S2 – S4)). Regarding the spectra it is important to note that a distortion cluster was added for all evaluations for the sake of comparability. The algorithm assigns spectra to the clusters automatically. In the case of measurements with generally high transmission, mostly pixels in the watery region are assigned to the "distortion" cluster, thus leading to a high similarity between the averaged spectra of the two clusters. For the images here, the diameters which can be determined also differ depending on the evaluation method. The diameter of the polyester fiber can be determined to be 21 µm using the transmission map and 15 µm using the FCM cluster map. For linen, those are 23 µm and 17 µm, and for wool 40 µm and 28 µm. The diameters of single threads of fabric were not cross-checked using a caliper here. The sample preparation results in further disintegration of the threads, therefore the diameters of the microfibers are not expected to be in the same range as those of single threads.

Raman maps for a mixture of two fibers– polyester and nylon– are shown in Fig. 7. It is important to note that, as the nylon fibers used here have a much larger diameter than the polyester ones and the fibers are positioned on top of each other, there is no focal plane yielding good signal for both fibers simultaneously. Similar to the case described above with one fiber positioned only partially in the focal plane (cf. Fig. 4), here a second fiber lies within the scanned region, partially or mostly outside of the focal plane. Therefore, measurements of the same sample region for two focal planes are shown. For one Raman map shown (Fig. 7 (a)), the nylon fiber appears less defined due to the lower signal. Not all sample positions lie in the focal plane, resulting in lower signal levels and a lower likelihood of the respective spectra to be grouped in that cluster. A lower intensity of the color is the consequence as well as low signal levels for the averaged cluster spectrum. A distinction between two types of fibers is still possible within *one* focal plane by the FCM cluster. The FSRM images for the same sample region but recorded on a different focal plane (Fig. 7(b)) yield a different result; there, the nylon fiber is better visible than the polyester fiber. However, in both FCM cluster images displayed on the right side of Fig. 7, the edges of the fibers within the focal plane seem to be classified as belonging to the other fiber. This occurs because reduced transmission at the fiber edges increases noise levels. For out-of-focus fibers, the Raman spectra are dominated by noise, which is also reflected in the spectral descriptors. Consequently, the FCM algorithm groups the out-of-focus fiber and the out-of-focus edges of the focused fiber into the same cluster. Corresponding averaged cluster spectra can be found in the Supporting Information Fig. S5.

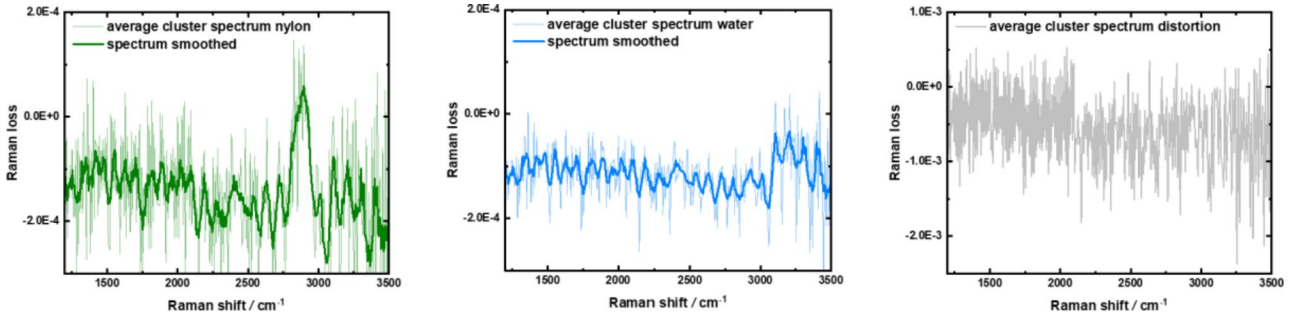


**Fig. 5** Averaged spectra of the assigned FCM clusters of the Raman maps shown in Fig. 2. All spectra assigned to one cluster were averaged and smoothed using a Savitzky Golay filter with a window size of 10 spectral pixels. Compared to Fig. 4, a smaller spectral range was selected as for wavenumbers < 1200 $cm^{-1}$ the noise exceeds the signal

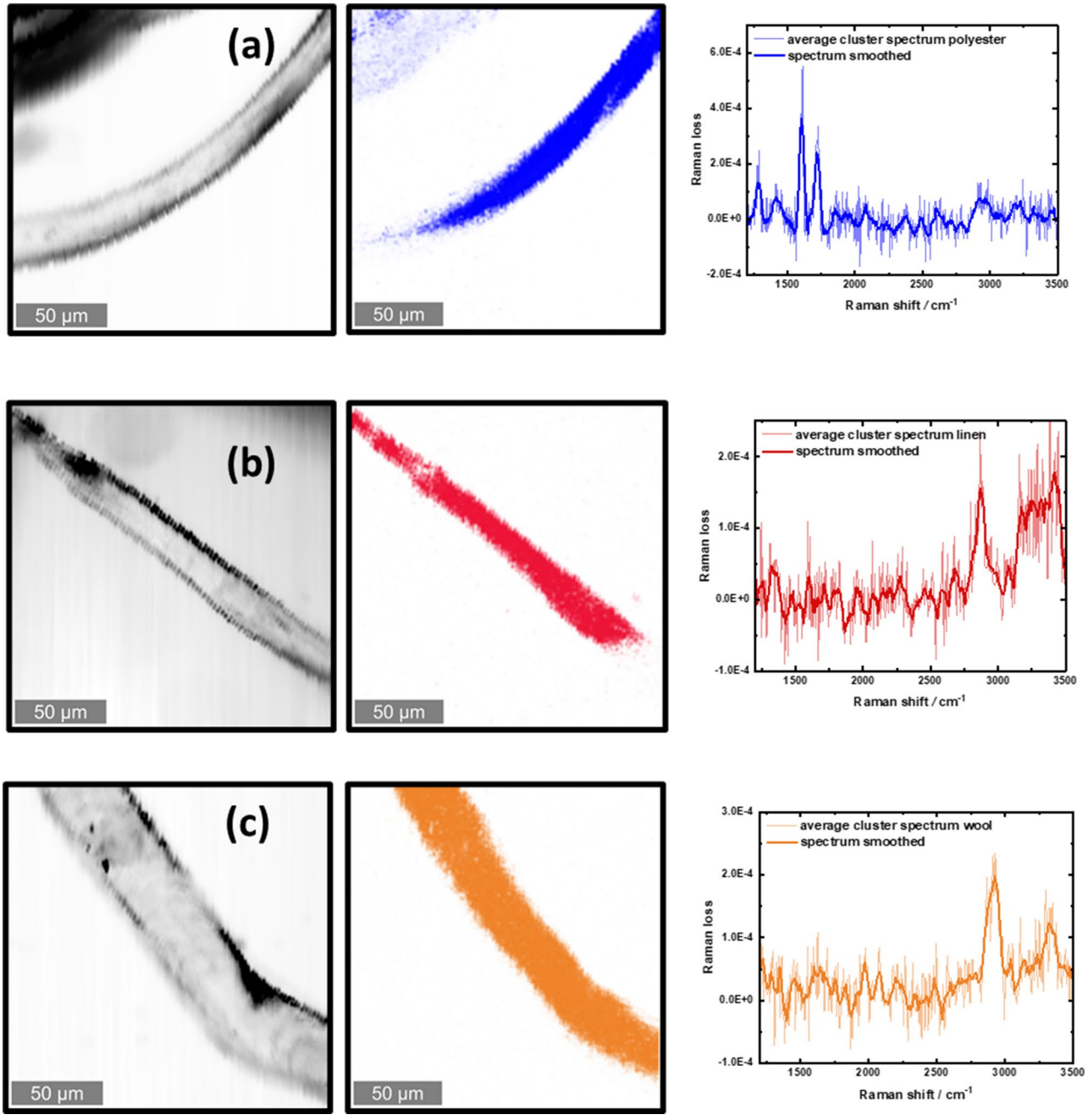


**Fig. 6** FSRM imaging of reference fibers polyester (**a**), linen (**b**), and wool (**c**) dispersed in water. Acquisition of the 200 × 200 µm maps with a spatial resolution of 1 µm and acquisition times of 10 ms/spectrum (corresponding to 100 averaged spectra per pixel) took ~ 7 min. Transmission maps (left) show the average transmission of the whole probe spectral range, with darker colors indicating lower transmission. In the false-color images (center), the likelihood of the spectra of each pixel to be assigned to the respective cluster is color-coded. The corresponding averaged Raman spectra of the reference fiber clusters (right) were smoothened using a Savitzky-Golay filter with a window size of 10 spectral pixels

## FSRM measurements of denim fabric

Denim is a fabric woven with blue as well as white threads. As described above, separate spectra were recorded in a single position as a reference. According to the label, it was expected to find spectra of cotton and polyester. The spectrum recorded of a white thread depicted in Fig. 8 (a) shows the Raman bands expected for cotton, which consists of cellulose like linen. For transmissive samples displaying only SRS, de-focusing solely leads to an increase in noise and decrease in signal. However, for the blue threads, strong non-linear effects were observed in form of baseline shifts depending on the focusing conditions (Fig. 8 (b)). This effect might be attributed for example to transient absorption or

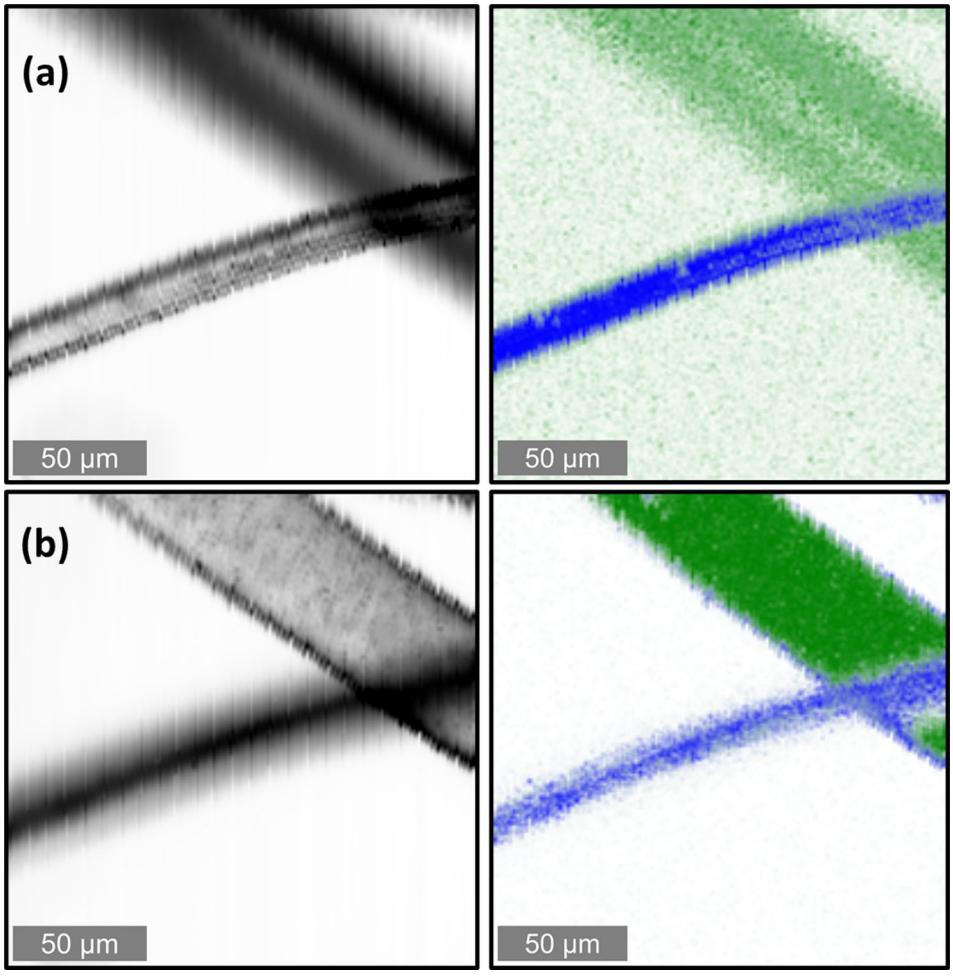


**Fig. 7** FSRM imaging of nylon (green) and polyester (blue) fibers for different focal planes. Acquisition of the 200 × 200 µm maps with a spatial resolution of 1 µm and acquisition times of 10 ms/spectrum (corresponding to 100 averaged spectra per pixel) took ~ 7 min. For both images, the transmission (left) and false-color FCM cluster image (right) display two fibers visible in the scanned region. In the top images (**a**), the smaller fiber (polyester) is within the focal plane, in the bottom images (**b**) the bigger fiber (nylon) is focused on. The two fibers can be attributed to polyester and nylon, as can be seen from the clusters' respective averaged Raman spectra provided in Supporting Information (Fig. S5)

cross-phase modulation due to higher non-linear refractive index of the blue dye molecules. For one focus condition (focus 4), two distinct bands can be discerned. These bands may correspond to the aromatic CC and C = O stretching Raman bands characteristic of polyester, albeit shifted to lower wavenumbers. This shift may result from incorrect focusing conditions. This could indicate that the blue denim fibers are composed of polyester but a correct assignment is not possible due to the distorted spectra.

Pieces of fabric were therefore bleached with NaOCl as described above until the fabric was visually discolored. For the following measurements of the bleached fibers, no such baseline distortions were observed. The Raman spectrum which can be attributed to cotton is not considerably altered by the bleaching. More important, Raman spectra and Raman maps of polyester without a perceived baseline shift due to non-linear effects added by the blue dye could be recorded, as shown in Figs. 9 and 10, respectively. Additionally, the previously observed spectral shift in the Raman bands is no longer evident. Thus, the two main components of the denim fabric, cotton and polyester, can be clearly distinguished in Raman maps after bleaching.

For both measurements shown, two fibers can be discerned by the transmission image, whereas one can be discerned by the false-color FCM Raman image. The corresponding averaged cluster spectra on the right side can be attributed to polyester and cotton. For evaluation of the polyester map (Fig. 10(a)), four clusters were selected as the out-of-focus fiber yielded a distortion cluster which is distinguishable from other regions with lower transmission. This resulted in better visualization. Evaluation of the map containing cotton (Fig. 10(b)) was performed as described for samples before using three clusters for the FCM algorithm as the out-of-focus fiber

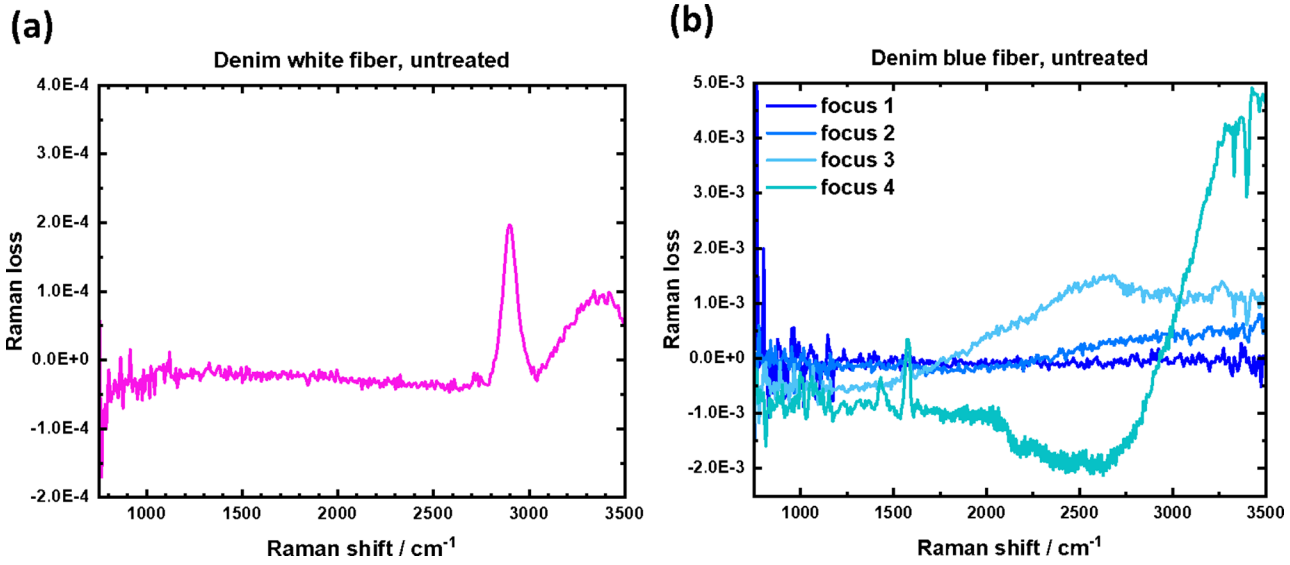


**Fig. 8** FSRM Raman spectra of white (left) and blue (right) denim fibers without bleaching. Acquisition time: 1 s/spectrum (corresponding to 10,000 averaged spectra). For the blue fiber, different focusing conditions at the same sample position led to different baseline shifts, which can be attributed to non-linear effects other than stimulated Raman scattering. For focus condition 4, two Raman peaks were observed

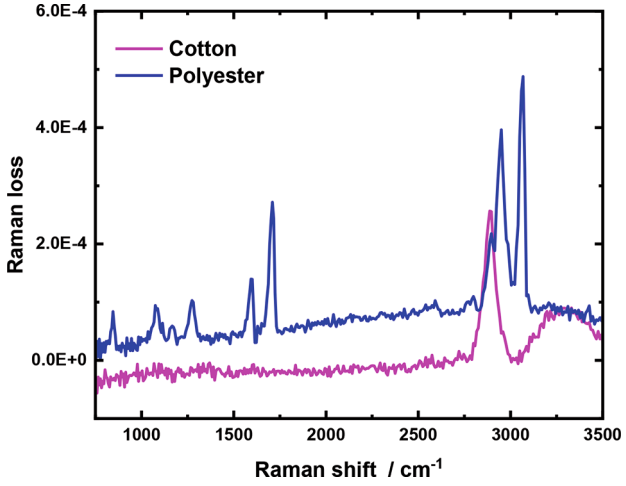


**Fig. 9** FSRM Raman spectra of cotton and polyester fibers of bleached denim fabric. Acquisition time: 1 s/spectrum (corresponding to 10,000 averaged spectra)

was not found to affect calculation of the distortion cluster. Corresponding averaged cluster spectra for water and distortion for both images can be found in Supporting Information (Fig. S6).

## Discussion

FSRM was employed for the characterization of microfibers in water. With the current modalities and sample preparation, a spectral coverage of 1250–3500 $cm^{-1}$ is achieved with a 10 ms/pixel acquisition time and an average spectral resolution of ~30 $cm^{-1}$ in that region. At present, for wavenumbers smaller than ~1250 $cm^{-1}$, the noise exceeds the signal due to a low probe light flux. A Raman map of 200 × 200 µm with 1 µm step size (i.e. 40,000 spectra) is recorded within ~7 min. This corresponds to an average acquisition time of 10.5 ms/pixel when also accounting for the time needed to scan the sample. For each spectrum, 512 spectral pixels are recorded. Transmission images can be computed from the same data recorded for acquisition of a Raman map without the need of an additional measurement. The spatial resolution of FSRM is ~1 µm. Under the chosen conditions, particles in a size range of ~10–200 µm can be characterized within one measurement. For particles smaller than 10 µm, distortions caused by refractive index mismatches between particle and matrix [62] render a precise size determination and characterization challenging. Minimum particle sizes for full Raman spectral maps reported before were around 5 µm [13, 28, 30], thus comparable to the minimal size reported in this study.

Recording times in Raman microscopy mostly depend on pixel acquisition times. Those of FSRM imaging reported here will now be compared with other Raman studies on microplastics. Like FSRM, conventional Raman microscopy offers complete spectral coverage. Typical acquisition times for microplastic analysis with the conventional approach were compiled by Araujo et al. [30] and are of the order of 1 s. A study of Elert et al. [63] stands out from the others with a reported acquisition time as short as 20 ms, i.e. twice the time required for presented images here. However, Raman spectra shown were recorded in chosen sample positions with acquisition times of the order of 10 s. Furthermore, scans of the area of 200 × 190 µm with 1 µm steps required a total acquisition time of ~35 min. This equals an average

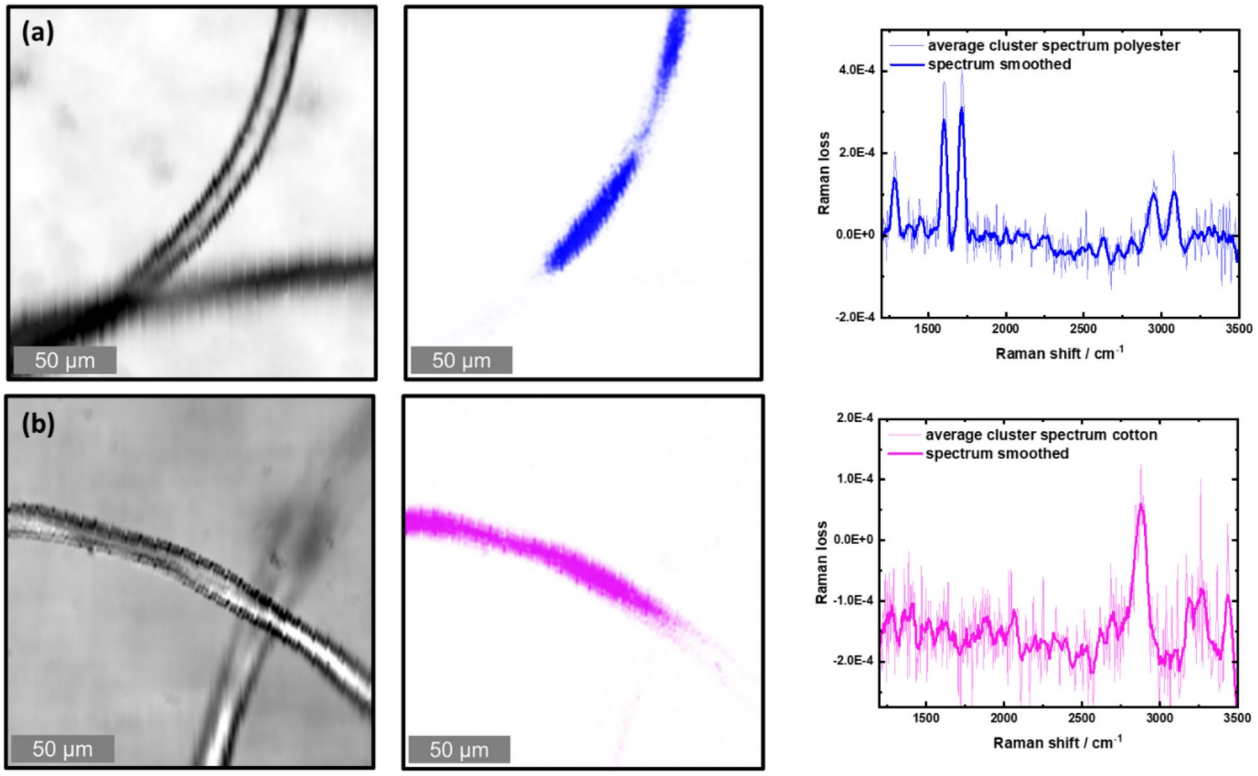


**Fig. 10** FSRM imaging of bleached denim fabric. Acquisition of the 200 × 200 µm maps with a spatial resolution of 1 µm and acquisition times of 10 ms/spectrum (corresponding to 100 averaged spectra per pixel) took ~ 7 min. Both measurements show different regions of the same sample, showing a polyester (**a**) and cotton (**b**) fiber. The corresponding averaged Raman spectra of the fiber clusters (right) were smoothened using a Savitzky-Golay filter with a window size of 10 spectral pixels

acquisition time of 55 ms/pixel when considering the scanning speed.

For a setup based on conventional SRS, recording a Raman map for one wavenumber over an area of 1 $cm^2$ with 2 µm steps was reported to require 40 min [25, 42], corresponding to a theoretical acquisition time of ~ 0.1 ms/pixel. This is equal to the lowest acquisition time per pixel possible for full coverage with FSRM, albeit not applied here due to insufficient Raman signal of the fibers. Raman mapping with a full spectral coverage (512 spectral pixels) reported here took only a factor of 100 longer than this single channel imaging. To obtain complete Raman spectra with a resolution of 3 $cm^{-1}$, Laptenok et al. [42] and Genchi et al. [25] tuned the frequency difference of the laser pulses (cf. Fig. 1). Acquiring the spectra took ~ 60 s. In comparison, a reference spectrum for one position is recorded *via* FSRM within 1 s in the vibrational range 750–3500 $cm^{-1}$ and with a resolution of 30 $cm^{-1}$. As mentioned above, the SNR would allow for a much lower acquisition time, e.g. 10 ms (cf. Fig. S1).

Zada et al. reported a measurement time of 4.5 h for a 1 $cm^2$ area scanned in 3 µm steps for 6 separate wavenumbers using SRS microscopy [40]. This is equal to a theoretical pixel acquisition time of ~ 0.15 ms. Here, the time between separate measurements to tune the wavenumbers is included. A single wavenumber map composed of 1024 × 1024 pixels is acquired within 22.45 s [41], resulting in an average pixel acquisition time of 0.02 ms. The required wavenumber tuning is a limiting factor not affecting FSRM.

Another essential factor which influences the quality of vibrational (micro-)spectroscopy is the SNR. The values of SNR are rarely reported in publications but can be estimated here by calculating the ratio between the signal of the strongest Raman band and the approximate noise level deduced from the fluctuations around the respective baselines. This estimation enables a rough comparison of spectra of the same substances.

For the results discussed above [25, 63], full Raman spectra have only been reported for single point measurements. Thus, the FSRM spectra shown in Fig. 2, recorded within an acquisition time of 1 s, are compared to these results, as they were recorded under similar conditions. Unsmoothed spectra for comparison are available for polyester, linen and wool. The $SNR_{1\,s}$ (according to the above definition and an acquisition time of 1 s) for polyester is 60. For linen, the value is 7, and for wool it is 15.

In the spontaneous Raman spectrum of the polyester polyethylene terephthalate [63], the SNR is estimated to

be 34 for a total acquisition time of 150 s. Assuming SNR to scale with the acquisition time $t_{at}$ according to SNR ~ $\frac{1}{\sqrt{t_{at}}}$ [64], an $SNR_{1\,s}$ of ~ 3 results. Thus, the $SNR_{1\,s}$ for the polyester spectrum recorded with the FSRM instrument is substantially higher. As a commercial setup was used for the spontaneous Raman spectrum, the comparison should therefore be representative for other spontaneous setups as well. For an SRS application, Genchi et al. [25] reported spectra of several compounds recorded with a 60 s acquisition time. The estimated SNRs are 76 ($SNR_{1\,s}$ ~ 10) for polyester, 39 ($SNR_{1\,s}$ ~ 5) for an animal fiber (likely keratin, similar to wool), and 43 ($SNR_{1\,s}$ ~ 6) for cellulose (the main component of linen). Thus, the $SNR_{1\,s}$ values for the FSRM setup are higher than those reported for an SRS instrument.

In terms of disturbing fluorescence, FSRM performs comparable to other SRS approaches, which are inherently unaffected. These approaches are, thus, advantageous over spontaneous Raman approaches. However, as FSRM and SRS measurements are carried out in transmission, dark or generally non-transmissive samples cannot be characterized. Some dyes can also cause nonlinear effects, resulting in a necessity to bleach samples. Konings et al. reported a deep-UV Raman excitation to enable measuring samples containing carbon black in addition to using SRS for particle characterization [41]. Genchi et al. further reported damage to environmental samples during the scanning caused by high laser powers [25]. The damaged fibers were partially assigned to be of natural origin. As FSRM operates at low laser powers, damage to samples is unlikely [45].

## Conclusions

This study introduces FSRM as a fast, broadband approach for destruction- and label-free analysis of microfibers. FSRM enables a simultaneous quantitative and qualitative evaluation of particles present in an aqueous sample without necessary prior knowledge of its constituents. We have shown that for the samples employed here, which were selected because they represent the most common types of fibers, FSRM can distinguish between natural and synthetic fibers. As a Raman map with full spectral coverage for each pixel is recorded for a chosen sample region, different components can be distinguished in the same scanned sample region. With the help of a spectral database, environmental samples can be evaluated in the future, as no prior measurements are necessary for evaluation of the chemical constituents of a sample. In this manner, the fast method of FSRM has the potential to accelerate measurements of microfibers as well as their evaluation. Continuing improvements in the setup and sample preparation process will further increase these capabilities. We aim to extend FSRM's application in microfiber analysis to the evaluation of effluent water of washing machines.

## Supplementary Information

The online version contains supplementary material available at https://doi.org/10.1186/s43591-025-00113-0.

Supplementary Material 1

**Acknowledgements**
Not applicable.

**Author contributions**
C.B.: Conceptualization, methodology, software, data curation, visualization, and writing– original draft; F.v.R.N.: methodology, software, visualization, and writing– review and editing; R.B.: methodology, software, formal analysis, and visualization; P.G.: conceptualization, supervision, and writing– review and editing.

**Funding**
Open Access funding enabled and organized by Projekt DEAL.
Not applicable.

**Data availability**
The datasets used and/or analysed during the current study are available from the corresponding author on reasonable request.

## Declarations

**Ethics approval and consent to participate**
Not applicable.

**Consent for publication**
Not applicable.

**Competing interests**
The authors declare no competing interests.

Received: 20 September 2024 / Accepted: 21 January 2025
Published online: 24 March 2025

**References**

1. Geyer R, Jambeck JR, Law KL. Production, use, and fate of all plastics ever made. Sci Adv. 2017;3(7):e1700782. https://doi.org/10.1126/sciadv.1700782.
2. OECD, Global Plastics O. 2022. https://doi.org/10.1787/aa1edf33-en
3. Andrady AL, Neal MA. Applications and societal benefits of plastics. Philos Trans R Soc B: Biol Sci. 2009;364(1526):1977–84. https://doi.org/10.1098/rstb.2008.0304.
4. Arthur C, Baker JE, Bamford HA. Proceedings of the International Research Workshop on the Occurrence, Effects, and Fate of Microplastic Marine Debris, September 9–11, 2008, University of Washington Tacoma, Tacoma, WA, USA; 2009. https://repository.library.noaa.gov/view/noaa/2509/noaa_2509_DS1.pdf
5. Thompson RC, Olsen Y, Mitchell RP, Davis A, Rowland SJ, John AW, et al. Lost at sea: where is all the plastic? Science. 2004;304(5672):838–838. https://doi.org/10.1126/science.1094559.
6. Carpenter EJ, Smith KL. Plastics on the Sargasso Sea Surface. Science. 1972;175(4027):1240–1. https://doi.org/10.1126/science.175.4027.1240.
7. Allen S, Allen D, Phoenix VR, Le Roux G, Durántez Jiménez P, Simonneau A, et al. Atmospheric transport and deposition of microplastics in a remote mountain catchment. Nat Geosci. 2019;12(5):339–44. https://doi.org/10.1038/s41561-019-0335-5.
8. Bergmann M, Mützel S, Primpke S, Tekman MB, Trachsel J, Gerdts G. White and wonderful? Microplastics prevail in snow from the Alps to the Arctic. Sci Adv. 2019;5(8):eaax1157. https://doi.org/10.1126/sciadv.aax1157.

9. Browne MA, Crump P, Niven SJ, Teuten E, Tonkin A, Galloway T, et al. Accumulation of microplastic on shorelines woldwide: sources and sinks. Environ Sci Technol. 2011;45(21):9175–9. https://doi.org/10.1021/es201811s.
10. Goßmann I, Herzke D, Held A, Schulz J, Nikiforov V, Georgi C, et al. Occurrence and backtracking of microplastic mass loads including tire wear particles in northern Atlantic air. Nat Commun. 2023;14(1):3707. https://doi.org/10.1038/s41467-023-39340-5.
11. Eriksen M, Lebreton LCM, Carson HS, Thiel M, Moore CJ, Borerro JC, et al. Plastic Pollution in the World's oceans: more than 5 trillion plastic pieces weighing over 250,000 tons afloat at Sea. PLoS ONE. 2014;9(12):e111913. https://doi.org/10.1371/journal.pone.0111913.
12. Liebezeit G, Liebezeit E. Synthetic particles as contaminants in German beers. Food Addit. 2014;31(9):1574–8. https://doi.org/10.1080/19440049.2014.945099.
13. Schymanski D, Goldbeck C, Humpf H-U, Fürst P. Analysis of microplastics in water by micro-raman spectroscopy: release of plastic particles from different packaging into mineral water. Water Res. 2018;129:154–62. https://doi.org/10.1016/j.watres.2017.11.011.
14. Bai C-L, Liu L-Y, Hu Y-B, Zeng EY, Guo Y, Microplastics. A review of analytical methods, occurrence and characteristics in food, and potential toxicities to biota. Sci Total Environ. 2022;806:150263. https://doi.org/10.1016/j.scitotenv.2021.150263.
15. Leslie HA, van Velzen MJ, Brandsma SH, Vethaak D, Garcia-Vallejo JJ, Lamoree MH. Discovery and quantification of plastic particle pollution in human blood. Environ Int. 2022;107199. https://doi.org/10.1016/j.envint.2022.107199.
16. Ragusa A, Svelato A, Santacroce C, Catalano P, Notarstefano V, Carnevali O, et al. Plasticenta: first evidence of microplastics in human placenta. Environ Int. 2021;146:106274. https://doi.org/10.1016/j.envint.2020.106274.
17. Liu S, Liu X, Guo J, Yang R, Wang H, Sun Y, et al. The association between microplastics and microbiota in placentas and meconium: the first evidence in humans. Environ Sci Technol. 2022. https://doi.org/10.1021/acs.est.2c04706.
18. Ragusa A, Notarstefano V, Svelato A, Belloni A, Gioacchini G, Blondeel C, et al. Raman Microspectroscopy Detection and Characterisation of Microplastics in Human Breastmilk. Polym. 2022;14(13):2700. https://doi.org/10.3390/polym14132700.
19. Jenner LC, Rotchell JM, Bennett RT, Cowen M, Tentzeris V, Sadofsky LR. Detection of microplastics in human lung tissue using μFTIR spectroscopy. Sci Total Environ. 2022;831:154907. https://doi.org/10.1016/j.scitotenv.2022.154907.
20. Amato-Lourenço LF, Carvalho-Oliveira R, Júnior GR, dos Santos Galvão L, Ando RA, Mauad T. Presence of airborne microplastics in human lung tissue. J Hazard Mater. 2021;416:126124. https://doi.org/10.1016/j.jhazmat.2021.126124.
21. Gaspar L, Bartman S, Coppotelli G, Ross JM. Acute exposure to Microplastics Induced changes in behavior and inflammation in Young and Old mice. Int J Mol Sci. 2023;24(15). https://doi.org/10.3390/ijms241512308.
22. Burns EE, Boxall AB. Microplastics in the aquatic environment: evidence for or against adverse impacts and major knowledge gaps. Environ Toxicol Chem. 2018;37(11):2776–96. https://doi.org/10.1002/etc.4268.
23. Boucher J, Friot D. Primary microplastics in the oceans: a global evaluation of sources. Vol. 10. Gland, Switzerland IUCN. 2017. https://doi.org/10.2305/IUCN.CH.2017.01.en.
24. Textile Exchange. Materials Market Report 2023. 2023. https://textileexchange.org/knowledge-center/reports/materials-market-report-2023/. Accessed 06 Jun 2024.
25. Genchi L, Martin C, Laptenok SP, Baalkhuyur F, Duarte CM, Liberale C. When microplastics are not plastic: Chemical characterization of environmental microfibers using stimulated Raman microspectroscopy. Sci Total Environ. 2023;164671. https://doi.org/10.1016/j.scitotenv.2023.164671.
26. Wiesheu AC, Anger PM, Baumann T, Niessner R, Ivleva NP. Raman microspectroscopic analysis of fibers in beverages. Anal Methods. 2016;8(28):5722–5. https://doi.org/10.1039/C6AY01184E.
27. Hidalgo-Ruz V, Gutow L, Thompson RC, Thiel M. Microplastics in the marine environment: a review of the methods used for identification and quantification. Environ Sci Technol. 2012;46(6):3060–75. https://doi.org/10.1021/es2031505.
28. Käppler A, Fischer D, Oberbeckmann S, Schernewski G, Labrenz M, Eichhorn K-J, et al. Analysis of environmental microplastics by vibrational microspectroscopy: FTIR, Raman or both? Anal Bioanal Chem. 2016;408(29):8377–91. https://doi.org/10.1007/s00216-016-9956-3.
29. Gao X, Li X, Min W. Absolute stimulated Raman Cross sections of molecules. J Phys Chem Lett. 2023;14(24):5701–8. https://doi.org/10.1021/acs.jpclett.3c01064.
30. Araujo CF, Nolasco MM, Ribeiro AM, Ribeiro-Claro PJ. Identification of microplastics using Raman spectroscopy: latest developments and future prospects. Water Res. 2018;142:426–40. https://doi.org/10.1016/j.watres.2018.05.060.
31. Li Z, Deen MJ, Kumar S, Selvaganapathy PR. Raman Spectroscopy for In-Line. Water Qual Monitoring—Instrumentation Potential Sens. 2014;14(9):17275–303. https://doi.org/10.3390/s140917275.
32. Thygesen LG, Løkke MM, Micklander E, Engelsen SB. Vibrational microspectroscopy of food. Raman vs. FT-IR. Trends Food Sci. 2003;14(1–2):50–7. https://doi.org/10.1016/S0924-2244(02)00243-1.
33. Meschede D. Optics, light and lasers: the practical approach to modern aspects of photonics and laser physics. 3rd ed. Wiley; 2017.
34. Freudiger CW, Min W, Saar BG, Lu S, Holtom GR, He C, et al. Label-free biomedical imaging with high sensitivity by stimulated Raman scattering microscopy. Science. 2008;322(5909):1857–61. https://doi.org/10.1126/science.1165758.
35. Rigneault H. In: Cheng J-X, Min W, Ozeki Y, Polli D, editors. Chapter 1 - coherent Raman scattering processes. Stimulated Raman Scattering Microscopy: Elsevier; 2022. pp. 3–20.
36. Ploetz E, Laimgruber S, Berner S, Zinth W, Gilch P. Femtosecond stimulated Raman microscopy. Appl Phys B. 2007;87(3):389–93. https://doi.org/10.1007/s00340-007-2630-x.
37. Kukura P, McCamant DW, Mathies RA. Femtosecond stimulated Raman Spectroscopy. Annu Rev Phys Chem. 2007;58(1):461–88. https://doi.org/10.1146/annurev.physchem.58.032806.104456.
38. Dietze DR, Mathies RA, Femtosecond Stimulated Raman. Spectrosc ChemPhysChem. 2016;17(9):1224–51. https://doi.org/10.1002/cphc.201600104.
39. McCamant DW, Kukura P, Mathies RA. Femtosecond broadband stimulated Raman: a new approach for high-performance vibrational spectroscopy. Appl Spectrosc. 2003;57(11):1317–23. https://doi.org/10.1366/0003702033225544 55.
40. Zada L, Leslie HA, Vethaak AD, Tinnevelt GH, Jansen JJ, de Boer JF, et al. Fast microplastics identification with stimulated Raman scattering microscopy. J Raman Spectrosc. 2018;49(7):1136–44. https://doi.org/10.1002/jrs.5367.
41. Konings MC, Zada L, Schmidt RW, Ariese F. Optimization of sample preparation, fluorescence-and Raman techniques for environmental microplastics. Spectrochim Acta A. 2024;124537. https://doi.org/10.1016/j.saa.2024.124537.
42. Laptenok SP, Martin C, Genchi L, Duarte CM, Liberale C. Stimulated Raman Microspectroscopy as a new method to classify microfibers from environmental samples. Environ Pollut. 2020;267:115640. https://doi.org/10.1016/j.envpol.2020.115640.
43. Yoshizawa M, Kurosawa M. Femtosecond time-resolved Raman spectroscopy using stimulated Raman scattering. Phys Rev A. 1999;61(1):013808. https://doi.org/10.1103/PhysRevA.61.013808.
44. Schrader B et al. Infrared and Raman spectroscopy: methods and applications. Weinheim VCH; 1995.
45. Lipkin M, Nixdorf J, Gilch P. Optimized amplitude modulation in femtosecond stimulated Raman microscopy. Opt Lett. 2020;45(15):4204–7. https://doi.org/10.1364/OL.397589.
46. Nixdorf J, Di Florio G, Bröckers L, Borbeck C, Hermes HE, Egelhaaf SU, et al. Uptake of methanol by poly (methyl methacrylate): an old problem addressed by a novel Raman technique. Macromol. 2019;52(13):4997–5005. https://doi.org/10.1021/acs.macromol.9b00205.
47. Opperskalski S, Franz A, Patanè A, Siew S, Tan E. Preferred Fiber & Materials Market Report 2022; 2022. http://textileexchange.org/app/uploads/2022/10/Textile-Exchange_PFMR_2022.pdf
48. Hedegaard M, Matthäus C, Hassing S, Krafft C, Diem M, Popp J. Spectral unmixing and clustering algorithms for assessment of single cells by Raman microscopic imaging. Theor Chem Acc. 2011;130:1249–60. https://doi.org/10.1007/s00214-011-0957-1.
49. Czerwinski L, Nixdorf J, Di Florio G, Gilch P. Broadband stimulated Raman microscopy with 0.1 ms pixel acquisition time. Opt Lett. 2016;41(13):3021–4. https://doi.org/10.1364/OL.41.003021.
50. Käppler A, Windrich F, Löder MG, Malanin M, Fischer D, Labrenz M, et al. Identification of microplastics by FTIR and Raman microscopy: a novel silicon filter substrate opens the important spectral range below 1300 cm−1 for FTIR transmission measurements. Anal Bioanal Chem. 2016;407(22):6791–801. https://doi.org/10.1007/s00216-015-8850-8.

51. Bottone A, Boily JF, Shchukarev A, Andersson PL, Klaminder J. Sodium hypochlorite as an oxidizing agent for removal of soil organic matter before microplastics analyses. J Environ Qual. 2021. https://doi.org/10.1002/jeq2.20321.
52. Palanisamy R, Rengarajan V, Sozhen G, Narasimham K. Electrolytic production of sodium hypochlorite for bleaching. IPPTA. 1993;5:45–45.
53. Bezdek JC, Ehrlich R, Full WFCM. The fuzzy c-means clustering algorithm. Comput Geosci. 1984;10(2–3):191–203. https://doi.org/10.1016/0098-3004(84)90020-7.
54. Carey DM, Korenowski GM. Measurement of the Raman spectrum of liquid water. J Chem Phys. 1998;108(7):2669–75. https://doi.org/10.1063/1.475659.
55. Howell NK, Arteaga G, Nakai S, Li-Chan EC. Raman spectral analysis in the C–H stretching region of proteins and amino acids for investigation of hydrophobic interactions. J Agric Food Chem. 1999;47(3):924–33. https://doi.org/10.1021/jf981074l.
56. Cho L-L. Identification of textile fiber by Raman Microspectroscopy. Forensic Sci. 2007;6:55–62.
57. Puchowicz D, Cieslak M. Raman spectroscopy in the analysis of textile structures. IntechOpen. 2022. https://doi.org/10.5772/intechopen.99731.
58. Rebollar E, Pérez S, Hernández M, Domingo C, Martín M, Ezquerra TA, et al. Physicochemical modifications accompanying UV laser induced surface structures on poly (ethylene terephthalate) and their effect on adhesion of mesenchymal cells. Phys Chem Chem Phys. 2014;16(33):17551–9. https://doi.org/10.1039/C4CP02434F.
59. Yoon S, McCamant DW, Kukura P, Mathies RA, Zhang D, Lee S-Y. Dependence of line shapes in femtosecond broadband stimulated Raman spectroscopy on pump-probe time delay. J Chem Phys. 2004;122(2). https://doi.org/10.1063/1.1828044.
60. Carter EA, Fredericks PM, Church JS, Denning RJ. FT-Raman spectroscopy of wool—I. preliminary studies. Spectrochim Acta A. 1994;50(11):1927–36. https://doi.org/10.1016/0584-8539(94)80205-X.
61. Prince RC, Frontiera RR, Potma EO. Stimulated Raman scattering: from bulk to nano. Chem Rev. 2017;117(7):5070–94. https://doi.org/10.1021/acs.chemrev.6b00545.
62. van der Kolk J, Lesina AC, Ramunno L. Effects of refractive index mismatch on SRS and CARS microscopy. Opt Express. 2016;24(22):25752–66. https://doi.org/10.1364/OE.24.025752.
63. Elert AM, Becker R, Duemichen E, Eisentraut P, Falkenhagen J, Sturm H, et al. Comparison of different methods for MP detection: what can we learn from them, and why asking the right question before measurements matters? Environ Pollut. 2017;231:1256–64. https://doi.org/10.1016/j.envpol.2017.08.074.
64. Traficante DD. Time averaging. Does the noise really average toward zero? Concepts Magn Reson. 1991;3(2):83–7. https://doi.org/10.1002/cmr.1820030203.


## Publisher's note